Porous triple network hydrogel humidity sensor with ultrafast response for wearable health monitoring

Shushu Chen(陈树澍), Tao Wang(王涛), Wenjin Luo(骆文瑾), Yunzheng Zhang(张允政), Jie Jiang(江杰), Liang Chen(陈亮)

Citation: Chin. Phys. B. 35, 100701 (2026). DOI: 10.1088/1674-1056/ae9e17 | CSTR: 32038.14.CPB.ae9e17
http://cpb.iphy.ac.cn; http://iopscience.iop.org/cpb

What follows is a list of articles you may be interested in

Electrocaloric thermal management devices: Toward high-efficiency solid-state refrigeration

Yiwen Bo(薄轶文), Rujun Ma(马儒军)
Chin. Phys. B. 35, 070701 (2026). DOI: 10.1088/1674-1056/ae3309 | CSTR: 32038.14.CPB.ae3309

Loading uniform Ag_3PO_4 nanoparticles on three-dimensional peony-like WO_3 for good stability and excellent selectivity towards NH_3 at room temperature

Xingyan Shao(邵星炎), Fuchao Jia(贾福超), Tingting Liu(刘婷婷), Jiancheng Liu(刘健诚), Xiaomei Wang(王小梅), Guangchao Yin(尹广超), Na Lv(吕娜), Tong Zhou(周通), Ramachandran Rajan, Bo Liu(刘波)
Chin. Phys. B. 32, 080703 (2023). DOI: 10.1088/1674-1056/ac98a0

Acetone sensors for non-invasive diagnosis of diabetes based on metal-oxide-semiconductor materials

Yujie Li(李育洁), Min Zhang(张敏), Haiming Zhang(张海明)
Chin. Phys. B. 29, 090702 (2020). DOI: 10.1088/1674-1056/aba60b

Coupling analysis of transmission lines excited by space electromagnetic fields based on time domain hybrid method using parallel technique

Zhi-Hong Ye(叶志红), Xiao-Lin Wu(吴小林), Yao-Yao Li(李尧尧)
Chin. Phys. B. 29, 090701 (2020). DOI: 10.1088/1674-1056/ab96a6

Design of NO_2 photoacoustic sensor with high reflective mirror based on low power blue diode laser

Hua-Wei Jin(靳华伟), Pin-Hua Xie(谢品华), Ren-Zhi Hu(胡仁志), Chong-Chong Huang(黄崇崇), Chuan Lin(林川), Feng-Yang Wang(王凤阳)
Chin. Phys. B. 29, 060701 (2020). DOI: 10.1088/1674-1056/ab8376

SPECIAL TOPIC — A 40th Anniversary Celebration: Physics Research and Innovation at Ningbo University

Porous triple network hydrogel humidity sensor with ultrafast response for wearable health monitoring

Shushu Chen(陈树澍)[†], Tao Wang(王涛)[†], Wenjin Luo(骆文瑾), Yunzheng Zhang(张允政), Jie Jiang(江杰)[‡], and Liang Chen(陈亮)

School of Physical Science and Technology, Ningbo University, Ningbo 315211, *China*

(Received 31 May 2026; revised manuscript received 6 August 2026; accepted manuscript online 25 August 2026)

The rapid advancement of flexible and wearable electronics calls for humidity sensors that combine mechanical compliance with high sensitivity and fast response. However, conventional rigid-substrate sensors cannot conformally attach to soft surfaces and often suffer from signal instability under deformation. Here, we report a porous conductive triple-network hydrogel humidity sensor designed through synergistic structural, electrical, and mechanical engineering. An interconnected microporous structure created by in situ CO_2 foaming accelerates water vapor transport. Carboxylated carbon nanotubes construct a uniform conductive network that enables efficient electrical signal transmission, whereas the triple-network matrix, integrated with covalent polyacrylamide crosslinks, sodium alginate–Ca^{2+} ionic coordination, and tannic acid–Fe^{3+} metal–phenolic interactions, effectively suppresses volumetric swelling and imparts outstanding mechanical stability. The sensor achieves a wide RH sensing range (11.3%–97.3% RH), an ultrafast response/recovery time of ≤ 0.144 s, and stable operation over 300 cycles. It successfully distinguishes different breathing patterns and pathways in real time and enables non-contact finger proximity detection at millimeter distances. This work provides a rational design strategy for high-speed wearable humidity sensors and intelligent non-contact interfaces.

Keywords: porous hydrogel, triple-network hydrogel, humidity sensor, carboxylated carbon nanotubes, fast response, respiratory monitoring

PACS: 07.07.Df, 82.70.Gg, 81.05.Qk

DOI: 10.1088/1674-1056/ae9e17 **CSTR:** 32038.14.CPB.ae9e17

1. Introduction

The rapid development of flexible and wearable electronics demands that humidity sensors possess multiple performance attributes, including flexibility, durability, high sensitivity, and fast response.[1,2] However, most commercially available resistive and capacitive humidity sensors are still fabricated on rigid substrates such as silicon and ceramics.[3] This makes it difficult to achieve effective conformal contact with soft, irregular surfaces, and they tend to suffer from signal drift or even failure under dynamic deformation. These limitations severely restrict their use in emerging applications that require intimate contact with the human body, such as respiration monitoring, skin moisture mapping, wound microenvironment assessment, and non-contact human–machine interaction.[3–7] As application scenarios impose increasingly strict requirements for both flexibility and signal stability, the inherent rigidity of existing commercial sensors has become a major bottleneck, highlighting the urgent need for new sensing materials that combine mechanical compliance with reliable humidity responsiveness.

Hydrogels, with their three-dimensional hydrophilic networks rich in polar groups and bound water, offer tissue-like softness, high deformability, and intrinsic moisture affinity, making them ideal candidates for next-generation humidity sensors.[8] Changes in ambient humidity dynamically modulate their hydration state, ionic mobility, interfacial polarization, and even volumetric swelling, which can be further transduced into electrical signals such as resistance, current, or capacitance.[9,10] Nevertheless, the direct use of conventional bulk hydrogels for humidity sensing faces three major bottlenecks: slow water vapor transport, weak electrical signal transduction, and poor mechanical stability. Specifically, the dense polymer network hinders water molecule adsorption and diffusion, leading to sluggish response/recovery that fails to capture rapid humidity fluctuations. Humidity-induced changes in the intrinsic ionic conductivity of hydrogels are often insufficient for efficient signal transduction, and the lack of efficient electronic conduction pathways leads to a poor signal-to-noise ratio. Under high humidity, excessive swelling not only disrupts the connectivity of the conductive network but also causes mechanical degradation, leaching of conductive fillers, and progressive signal deterioration over repeated swelling–drying cycles. Collectively, these issues constitute the core obstacles to the practical application of hydrogel-based humidity

[†]These authors contributed equally to this work.

[‡]Corresponding author. E-mail: jiangjie1@nbu.edu.cn

© 2026 Chinese Physical Society and IOP Publishing Ltd. All rights, including for text and data mining, AI training, and similar technologies, are reserved.

sensors.

To address these challenges, we adopt a synergistic design strategy from three perspectives: structural engineering, electrical transduction, and mechanical reinforcement. To accelerate water vapor transport, we construct an interconnected microporous architecture that increases the specific surface area and shortens the diffusion path of water molecules, thereby enhancing both sensitivity and response speed.[11–16] To improve electrical transduction, we introduce high-aspect-ratio carbon nanotubes (CNTs) as conductive fillers[17,18] and use their uniformly dispersed network to efficiently convert humidity-induced swelling and microstructural changes into reproducible electrical signals.[19,20] To ensure mechanical stability, we develop a multi-network system consisting of the covalent PAAm network, the SA–Ca^{2+} ionic network, and the TA–Fe^{3+} metal–phenolic coordination network. This system effectively suppresses swelling under high humidity, stabilizes the porous framework, and maintains the connectivity of conductive channels under repeated deformation.[21–24]

The resulting hydrogel humidity sensor integrates rapid water vapor transport channels, abundant hydrophilic adsorption sites, and an efficient ionic/electronic hybrid conductive network. Owing to the synergistic optimization of structure and materials, the sensor exhibits sensitive and distinguishable responses over a wide relative humidity range of 11.3%–97.3%, with response and recovery times of ≤ 0.144 s. It also maintains stable signal output over 300 consecutive humidity cycles. In addition, the sensor can distinguish different breathing patterns and airways in real time and achieve non-contact finger proximity detection at millimeter-scale distances. By combining porous structural design, dynamic network reinforcement for structural stabilization, and nanotube-mediated electrical transduction within a soft hydrogel platform, this work provides a viable technological pathway toward high-speed wearable humidity sensors and intelligent non-contact interfaces.

2. Materials and methods

2.1. Materials

Acrylamide (AAm), N, N′-methylenebisacrylamide (MBA), ammonium persulfate (APS), N, N, N′, N′-tetramethylethylenediamine (TEMED), polyethylene glycol (PEG-4000), sodium dodecyl sulfate (SDS), sodium bicarbonate ($NaHCO_3$), and citric acid were obtained from Shanghai Macklin Biochemical Co., Ltd. (Shanghai, China). Sodium alginate (SA), tannic acid (TA), anhydrous calcium chloride ($CaCl_2$), and ferric chloride hexahydrate ($FeCl_3{\cdot}6H_2O$) were obtained from Shanghai Aladdin Biochemical Technology Co., Ltd. (Shanghai, China). Concentrated nitric acid (HNO_3) and concentrated sulfuric acid (H_2SO_4) were obtained from Sinopharm Chemical Reagent Co., Ltd. (Shanghai, China). Pristine multi-walled carbon nanotubes (MWCNTs; $>$ 99% purity, outer diameter of 8–15 nm, length of 8–14 μm, and specific surface area of ≥ 250 $m^2{\cdot}g^{-1}$) were obtained from Shenzhen Suiheng Technology Co., Ltd. (Shenzhen, China). Lithium chloride (LiCl), magnesium chloride ($MgCl_2$), potassium carbonate (K_2CO_3), sodium chloride (NaCl), and potassium sulfate (K_2SO_4), which were used to establish the reference RH environments, were obtained from Aladdin. All chemical reagents were of analytical-reagent grade unless otherwise noted; the assay concentrations of concentrated HNO_3 and H_2SO_4 were 65–68 wt% and 95–98 wt%, respectively. Deionized water with a resistivity of 18 MΩ·cm at 25 °C was used throughout. All materials were used as received.

2.2. Preparation of carboxylated MWCNTs

To prevent aggregation and sedimentation of pristine MWCNTs and to facilitate the formation of a homogeneous, stable, and humidity-sensitive conductive network within the hydrogel matrix, we carboxylated the nanotubes before use. Briefly, 3 g of MWCNTs powder was gradually added to 130 mL of a mixed acid solution of concentrated HNO_3 and H_2SO_4 with a volume ratio of 1:3. The mixture was ultrasonically dispersed for 20 min and then stirred continuously at 80 °C in an oil bath for 2 h. After cooling to room temperature, the reaction mixture was diluted with deionized water to a final volume of 1 L and centrifuged at 10000 rpm for 30 min. The collected precipitate was redispersed in deionized water and dialyzed until neutral, yielding carboxylated MWCNTs. The introduction of carboxyl groups improved the aqueous dispersibility of the nanotubes and promoted their uniform incorporation into the hydrogel matrix.[25]

2.3. Preparation of PEG-assisted carboxylated MWCNTs dispersion

PEG-4000 (0.50 g) was dissolved in deionized water (5 mL) at 60 °C with magnetic stirring for 1 h until a clear and homogeneous solution was obtained. Complete dissolution of PEG-4000 was confirmed by placing a small drop of the solution on a glass plate and allowing it to cool to room temperature; no crystalline precipitate was observed. Carboxylated MWCNTs (0.03 g) and SDS (0.05 g) were then added to the PEG solution, and the mixture was ultrasonicated in an ice bath at 40 kHz and 100 W for 60 min to obtain a uniformly dispersed suspension of carboxylated MWCNTs.[26]

2.4. Fabrication of porous PAAm/carboxylated MWCNTs hydrogel

AAm (2.00 g) and MBA (0.04 g) were first dissolved in deionized water (5 mL) under magnetic stirring for 30 min

to obtain a homogeneous monomer solution. The PEG/SDS-assisted carboxylated MWCNTs dispersion was then added to the monomer solution and stirred thoroughly to ensure uniform distribution of the conductive nanotubes. Subsequently, APS (0.02 g) and $NaHCO_3$ (0.15 g) were sequentially introduced under continuous stirring until complete dissolution. An aqueous citric acid solution (0.10 g in 1 mL deionized water) was then added dropwise to trigger in situ CO_2 generation, which served as the foaming process for constructing the porous structure. Immediately afterward, TEMED (20 μL) was added, and the precursor was rapidly stirred for 10 s, poured into a mold, and cured at 40 °C for 5 min. The obtained porous PAAm/carboxylated MWCNTs hydrogel, without subsequent SA/TA infiltration or Fe/Ca post-crosslinking treatment, was defined as the pristine hydrogel and used as the control sample for subsequent structural and wettability comparisons.[27]

2.5. Preparation of SA/TA infiltration solution

SA (1.50 g) and TA (0.45 g) were dissolved in deionized water (30 mL) with magnetic stirring at 500 rpm for 1.5 h until a uniform solution was obtained. Mild heating at 40 °C was applied if needed to facilitate dissolution. SDS (0.30 g) was then added, and the mixture was stirred for another 15 min to obtain a transparent and homogeneous infiltration solution. The SA/TA mass ratio of 3.33:1 was selected because it produced the largest and most repeatable response among the tested ratios of 2:1, 3.33:1, and 5:1 (Fig. S1).

2.6. Construction of the ionic/coordination networks by SA/TA infiltration and post-crosslinking

The porous PAAm/carboxylated MWCNTs hydrogel was first left at room temperature for 10 min to complete initial gelation. It was then immersed in the SA/TA infiltration solution at 4 °C for 24 h to allow sufficient diffusion of SA and TA into the porous framework. After infiltration, the hydrogels were transferred into three different $FeCl_3{\cdot}6H_2O/CaCl_2$ post-crosslinking solutions to study the effect of the Fe/Ca ratio on the hydrogel structure and sensing performance. Specifically, for Group I, $FeCl_3{\cdot}6H_2O$ (0.9 g) and anhydrous $CaCl_2$ (0.1 g) were dissolved in 30 mL of deionized water, giving a nominal molar ratio of 3.7:1. For Group II, $FeCl_3{\cdot}6H_2O$ (0.7 g) and anhydrous $CaCl_2$ (0.3 g) were dissolved in 30 mL of deionized water, giving a nominal molar ratio of 1.0:1. For Group III, $FeCl_3{\cdot}6H_2O$ (0.5 g) and anhydrous $CaCl_2$ (0.5 g) were dissolved in 30 mL of deionized water, giving a nominal molar ratio of 0.4:1. After post-crosslinking at room temperature for 4 h, the hydrogels were washed three times with deionized water to remove residual free ions. Through this sequential treatment, the hydrogel matrix was transformed into a covalent/ionic/coordination triple-network structure consisting of the original PAAm covalent network, the SA–Ca^{2+} ionic network, and the TA–Fe^{3+} coordination network. In this work, the term "triple network" refers to the three deliberately constructed and dominant networks within the hydrogel matrix, including the covalent PAAm network, the SA–Ca^{2+} ionic network, and the TA–Fe^{3+} coordination network. Additional interactions, such as Fe^{3+}–SA and Ca^{2+}–TA interactions, may coexist in this multicomponent system but are regarded as secondary interactions rather than independent network structures. The resulting hydrogel was defined as the post-crosslinked hydrogel and was used for subsequent characterization and humidity-sensing measurements unless otherwise specified.[22,23]

2.7. Sensor assembly and humidity-sensing measurements

For sensor assembly, the prepared porous conductive hydrogel was cut into the desired shape and integrated with flexible copper tape electrodes in a sandwich configuration. The device consisted of a bottom Cu electrode, a porous hydrogel sensing layer, and a top patterned Cu electrode. The patterned upper electrode maintained electrical contact while allowing water vapor to access the hydrogel surface, whereas the bottom Cu electrode served as the counter/contact electrode. The assembled device was connected to a source meter, and the electrical signals were recorded at a constant bias voltage of 0.05 V.

Humidity sensing performance was evaluated under controlled relative humidity (RH) conditions generated by saturated salt solutions, namely 11.3%, 33.1%, 43.2%, 75.3%, and 97.3% RH. The relative response was calculated as

$$\Delta I/I_0\ (\%) = (I - I_0)/I_0 \times 100\%,$$

where I_0 is the baseline current and I is the current under the target humidity. Response and recovery times were defined as the time required to reach 90% of the full signal change during adsorption and desorption, respectively. The current was recorded at intervals of 0.144 s, and both the response and recovery reached the defined 90% criterion within the first sampling interval. Therefore, the response and recovery times are reported as ≤ 0.144 s, which represents the temporal resolution of the measurement system rather than the intrinsic response time of the sensor. Cycling stability was assessed by repeatedly switching the humidity between approximately 35% and 95% RH for 300 cycles over approximately 3000 s (50 min), with each humidification–dehumidification cycle lasting about 10 s. Respiratory and non-contact sensing tests were performed under ambient conditions by placing the device near the mouth or nose, or close to a finger without direct contact.[28]

3. Results and discussion

3.1. Structural design of the porous conductive triple-network hydrogel

As illustrated in Fig. 1(a), the hydrogel was fabricated via a stepwise process involving polymerization, foaming, infiltration, and post-crosslinking. First, acrylamide (AAm) underwent free-radical polymerization initiated by APS/TEMED and covalent crosslinking mediated by MBA, forming a stable PAAm network as the primary skeleton. Concurrently, the citric acid/$NaHCO_3$ foaming reaction generated CO_2 bubbles that were trapped during gelation, yielding an interconnected porous structure. Subsequently, sodium alginate (SA) and tannic acid (TA) diffused into the porous PAAm scaffold and served as precursors for secondary network formation. After post-treatment in a $FeCl_3{\cdot}6H_2O/CaCl_2$ solution, the carboxylate groups of SA formed an ionically crosslinked network with Ca^{2+} through the classical egg-box structure, while TA coordinated with Fe^{3+} to establish a dynamic metal–phenolic network. To ensure stable electrical signal transduction, carboxylated MWCNTs were introduced as conductive fillers. Carboxylation improved the aqueous dispersibility of the nanotubes, and the addition of PEG and SDS further suppressed re-aggregation, enabling a uniform distribution of MWCNTs throughout the precursor system.

In this work, the term "triple network" refers to the three deliberately constructed and dominant networks within the hydrogel matrix, including the covalent PAAm network, the SA–Ca^{2+} ionic network, and the TA–Fe^{3+} metal–phenolic coordination network. Additional interactions, such as Fe^{3+}–SA and Ca^{2+}–TA interactions, may coexist in this multicomponent system but are regarded as secondary ionic/coordination interactions rather than independent network structures, as they mainly contribute to interfacial reinforcement. Finally, the hydrogel layer was sandwiched between a bottom Cu electrode and a top patterned Cu electrode to form a flexible humidity sensor (Fig. 1(b)). This configuration ensures stable electrical contact, while the interdigitated upper electrode and the porous hydrogel surface allow efficient exposure to water vapor.

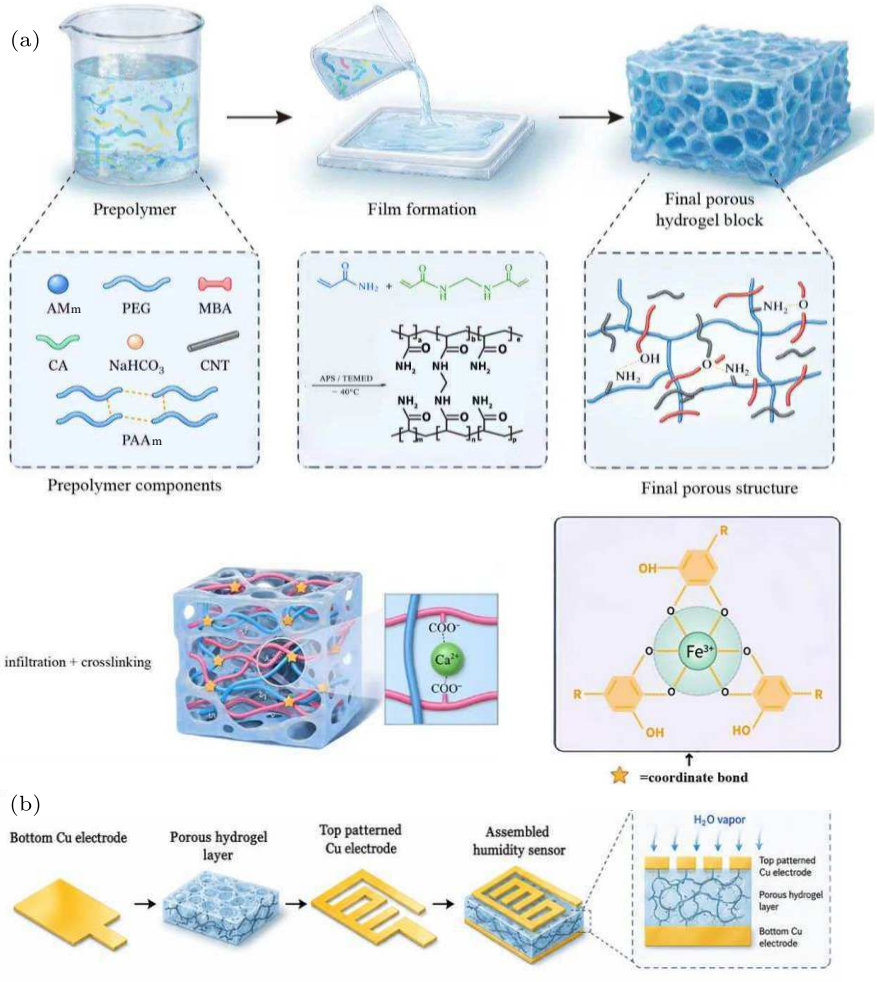

Fig. 1. (a) Fabrication scheme of the porous conductive triple-network hydrogel. (b) Device structure of the flexible humidity sensor.

3.2. Morphological and chemical characterization

The porous morphology of the hydrogels was examined by scanning electron microscopy (SEM). As shown in Fig. 2(a), both the pristine PAAm/carboxylated MWCNTs hydrogel and the post-crosslinked hydrogel exhibited open and interconnected porous architectures, providing continuous channels for water vapor transport. Compared with the pristine hydrogel (Fig. 2(a)(i)), the post-crosslinked hydrogel (Fig. 2(a)(i)) retained the porous framework, while its pore walls became thicker and the network skeleton became more compact and reinforced. Energy-dispersive x-ray spectroscopy (EDS) of the post-crosslinked hydrogel membrane further confirmed the successful incorporation of the post-crosslinking components (Fig. 2(b)). In addition to the dominant C, N, and O signals from the polymer matrix, clear Ca and Fe signals were detected in the post-crosslinked hydrogel. Elemental mapping (Fig. 2(c)) showed that Ca and Fe were distributed throughout the analyzed cross-section, supporting the incorporation of the post-crosslinking components in the imaged region. However, these data do not by themselves verify or quantify homogeneous ionic and coordination network formation throughout the entire hydrogel.

Surface wettability was evaluated by dynamic water contact angle measurements, as this parameter directly affects humidity adsorption and diffusion. As shown in Fig. 3(a)(i), the pristine hydrogel showed a water contact angle of 29.4° at 100 ms after droplet deposition, confirming its intrinsic hydrophilicity and rapid interaction with water molecules. Notably, after SA/TA infiltration and Fe/Ca post-crosslinking, the water droplet spread and permeated into the hydrogel surface almost immediately, giving an apparent contact angle close to 0° (Fig. 3(a)(ii)). This rapid wetting behavior is closely related to the post-crosslinked porous morphology: the interconnected pores increase the accessible interfacial area and facilitate liquid/vapor penetration; meanwhile, the introduced SA and TA provide abundant hydroxyl, carboxylate, and phenolic groups for water capture. Thus, the contact angle results, together with the SEM observations, demonstrate that the post-crosslinked hydrogel integrates a stable porous scaffold with substantially enhanced hydrophilicity, which benefits rapid water vapor adsorption, diffusion, and transport within the sensing layer.

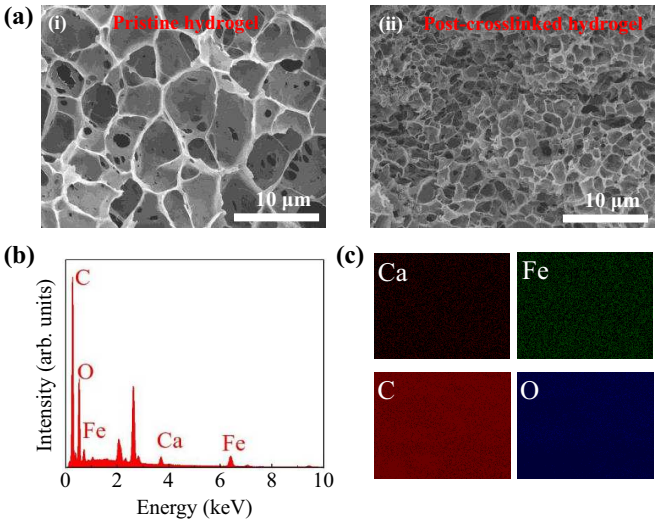

Fig. 2. (a) SEM images of the pristine (i) and post-crosslinked (ii) hydrogels; (b) EDS spectrum of the post-crosslinked hydrogel; (c) elemental mapping of the post-crosslinked hydrogel.

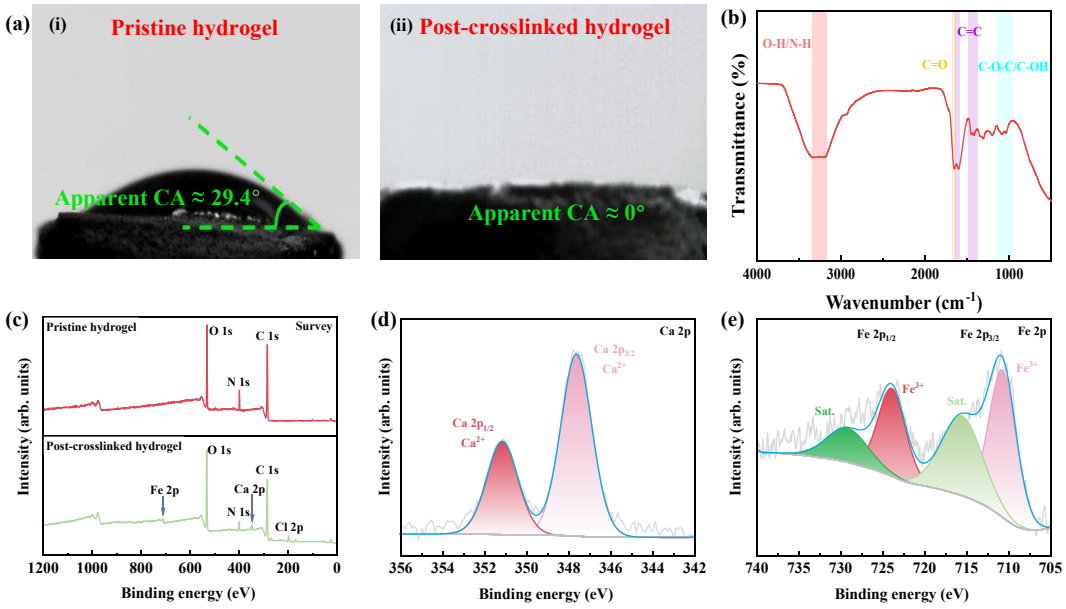

Fig. 3. (a) Dynamic water contact angles of the pristine (i) and post-crosslinked (ii) hydrogels; (b) FTIR spectrum of the post-crosslinked hydrogel; (c) XPS survey spectra of the pristine and post-crosslinked hydrogels; (d) high-resolution XPS spectrum of Ca 2p; (e) high-resolution XPS spectrum of Fe 2p.

Fourier-transform infrared spectroscopy (FTIR) identified the characteristic functional groups within the hydrogel. In the FTIR spectrum of the post-crosslinked hydrogel membrane (Fig. 3(b)), the broad bands at 3335 cm^{-1} and 3206 cm^{-1} were assigned to overlapping O–H and N–H stretching vibrations from PAAm, SA, TA, and bound water. The peak at 1651 cm^{-1} corresponded to the amide C=O stretching of PAAm, while the band at 1603 cm^{-1} was attributed to overlapping aromatic C=C stretching and asymmetric COO^- vibration. The peaks at 1456 cm^{-1} and 1423 cm^{-1} arose from $–CH_2–$ bending vibrations, and the band at 1310 cm^{-1} was associated with C–N or COO^--related vibrations. In addition, the peaks at 1201 cm^{-1}, 1089 cm^{-1}, and 1045 cm^{-1} were assigned to C–O and C–O–C stretching vibrations mainly derived from TA, SA, and PEG-related oxygen-containing groups. These characteristic signals confirm the coexistence of amide, hydroxyl, carboxylate, phenolic, and ether groups in the hydrogel network, providing abundant active sites for water molecule adsorption.

X-ray photoelectron spectroscopy (XPS) further confirmed the elemental composition. The survey spectrum of the pristine hydrogel mainly showed C 1s, N 1s, and O 1s signals from the PAAm network, carboxylated MWCNTs, and oxygen-containing components in the hydrogel matrix (Fig. 3(c)). After SA/TA infiltration and Fe/Ca post-crosslinking, distinct Fe 2p and Ca 2p signals appeared in the spectrum of the post-crosslinked hydrogel, confirming the successful introduction of Fe- and Ca-containing crosslinking species. Combining the SEM, contact angle, elemental mapping, FTIR, and XPS results, it can be confirmed that a hydrophilic, porous, and triple-network hydrogel has been successfully constructed.

3.3. Humidity-sensing performance

All measurements were conducted at a constant bias voltage of 0.05 V and a temperature of 25 °C, with the relative response defined as $\Delta I/I_0$ (%). We first investigated the effects of the Fe^{3+}/Ca^{2+} post-crosslinking ratio and the sensing layer thickness on humidity response. Among the three ratios tested (Fe^{3+}:Ca^{2+} = 3.7:1, 1:1, and 0.4:1), the equimolar sample (1:1) exhibited the strongest and most reproducible current response. The Fe-rich sample (3.7:1) gave a much weaker response, whereas the Ca-rich sample (0.4:1) showed an intermediate response. Additionally, under identical humidity-switching conditions, the double-network hydrogel exhibited a normalized response of approximately 170%, while the triple-network hydrogel reached approximately 280%, demonstrating that the TA–Fe^{3+} coordination network provides additional reinforcement and improves humidity response amplitude (Fig. S2). This result indicates that the humidity-sensing performance depends on a balance between coordination reinforcement and ionic network regulation, rather than simply increasing either type of crosslinking.

We then examined the influence of hydrogel thickness (0.5 mm, 0.8 mm, 1.0 mm, and 1.2 mm) on response kinetics (Fig. 4(b)). The 0.8 mm sensing layer delivered the shortest average response and recovery times. The thickness-dependent behavior may arise from multiple coupled factors, including vapor diffusion distance, water uptake,

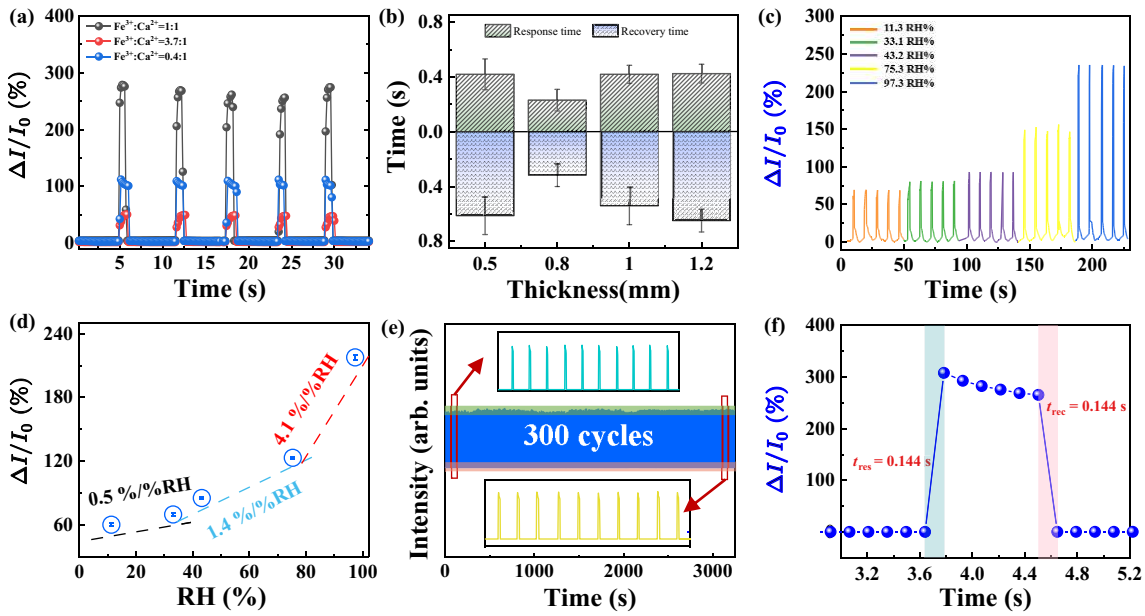

Fig. 4. (a) Current responses of the hydrogel sensors with different Fe^{3+}/Ca^{2+} post-crosslinking ratios (3.7:1, 1:1, and 0.4:1). (b) Response and recovery times of sensors with different thicknesses (0.5, 0.8, 1.0, and 1.2 mm). (c) Dynamic current responses of the optimized sensor upon exposure to various relative humidity levels (11.3%–97.3%). (d) Sensitivity curve of the sensor. (e) Long-term cycling stability of the sensor over 300 cycles between ∼ 35% and 95% RH. (f) Single-cycle response/recovery curve.

surface-to-volume ratio, thickness uniformity, electrode contact, and conductive pathway continuity. A thinner hydrogel layer provides a shorter diffusion distance and lower overall water content, which may contribute to faster humidity equilibration; however, its sensing performance may also be more sensitive to local thickness variation and interfacial contact conditions. In contrast, a thicker layer requires water transport through a longer diffusion path before reaching equilibrium. The present experiments do not allow quantitative separation of these individual contributions or identification of a single dominant cause. Based on these findings, all subsequent experiments were performed with a post-crosslinking ratio of Fe^{3+}:Ca^{2+} = 1:1 and a membrane thickness of 0.8 mm. Compression tests were performed on three independently prepared post-crosslinked hydrogel specimens. The stress–strain curves showed good reproducibility, and the compressive stress reached approximately 14–15 kPa at 50% strain (Fig. S3). Photographs of the hydrogel in its initial, stretched, folded, and knotted states are also provided in Fig. S3, qualitatively demonstrating its flexibility and macroscopic deformability.

The optimized sensor exhibited a clear humidity-dependent response over the entire tested RH range (Fig. 4(c)). As the relative humidity increased from 11.3% to 97.3%, the peak $\Delta I/I_0$ increased progressively. Repeated humidity pulses at each RH level generated highly similar signal profiles, confirming that the hydrogel sensor reversibly converts humidity variations into electrical output. The sensitivity curve further revealed a nonlinear response (Fig. 4(d)): the sensitivity increased from approximately 0.5 %/%RH in the low-humidity region to 1.4 %/%RH in the intermediate region, and further to 4.1 %/%RH in the high-humidity region. The accelerated signal rise at high RH suggests the gradual formation of more continuous water pathways within the hydrogel, which markedly enhances ion transport and conductive pathway modulation.

Long-term cycling stability was evaluated by repeatedly switching the sensor between approximately 35% and 95% RH (Fig. 4(e)). The device maintained stable and distinguishable current signals over 300 cycles, with no obvious signal failure or severe baseline drift, indicating that the porous conductive network can tolerate repeated adsorption–desorption processes. In addition, the sensor displayed ultrafast dynamic behavior under abrupt humidity changes. An enlarged single-cycle curve from Fig. 4(e) yielded response and recovery times of ≤ 0.144 s, demonstrating rapid water adsorption/desorption and prompt electrical transduction of vapor stimuli. Finally, we added a comparison table summarizing key performance parameters (response time, recovery time, and relative humidity range) from previous reports; the comparison shows that our sensor exhibits a shorter response time than those reported in the selected literature (Table 1).

Table 1. Comparison of humidity sensing performance between this work and previously reported sensors, including response time, recovery time, and relative humidity range.

Materials	RH range (%)	Response time (s)	Recovery time (s)	Reference
Porous PAAm/SA/TA/carboxylated-MWCNT triple-network hydrogel	11.3–97.3	≤ 0.144	≤ 0.144	This work
PAM/κ-carrageenan-EG/Gly double-network organohydrogel	4–90	0.270	0.300	Ref. [10]
Ultrathin transparent anti-freezing organohydrogel film	20–90	0.410	0.300	Ref. [29]
PAM/tapioca double-network hydrogel film	11–98	1.410	1.940	Ref. [9]
Crosslinked sodium alginate/MXene hydrogel	10–90	4.000	11.000	Ref. [30]
SA/PVA/glycerol conductive flexible hydrogel sponge (SPS@PVDF)	None	2.500	4.000	Ref. [31]
Ionically crosslinked gum tragacanth (GT) hydrogel film	0–97	5.500	43.300	Ref. [32]
Carrageenan-modified MXene nanocomposite (CAMX-2), all-printed on paper	11–97	4.600	5.800	Ref. [33]
MXene/LiCl/PAAm/PVA organic hydrogel	40–85	0.165	0.248	Ref. [34]
Aloe polysaccharide-based self-healing/freeze-resistant hydrogel	None	0.700	0.800	Ref. [35]
CaAlg hydrogel-coated tapered optical fiber	55–75	0.710	1.650	Ref. [36]
PNIPAM hydrogel-filled fiber Fabry–Perot cavity	45–75	0.910	1.910	Ref. [37]
Bilayer double-network hydrogel ionic skin	None	3.000	94.000	Ref. [38]
Ultrathin hierarchical hydrogel–carbon nanocomposite on PDMS	11–96	13.000	0.480	Ref. [39]
Droplet-enabled porous PVA/QD composite gel	11–93	43.000	46.000	Ref. [40]
Acrylic acid/bagasse cellulose/GO porous hydrogel	33.7–75.3	177.400	150.600	Ref. [41]
PAM/κ-carrageenan ion-conductive double-network hydrogel thin film	11–98	201.000	41.000	Ref. [42]
PVA–cellulose nanofiber organohydrogel film/biomimetic iontronics	11–98	380.000	140.000	Ref. [43]

3.4. Humidity-sensing mechanism

The rapid humidity switching is attributed primarily to the interconnected porous architecture and optimized sensing-layer thickness, which provide rapid channels for water vapor diffusion, while the polar groups in PAAm, SA, and TA facilitate water adsorption. The TA–Fe^{3+} coordination network is considered to contribute mainly to signal enhancement and structural stabilization rather than to faster vapor diffusion.

The measured electrical response is not caused by dif-

ferent ionization states between the two hydrogel surfaces. The sensor has a symmetric structure without intentionally designed surface asymmetry and is operated under an external bias voltage. Instead, the measured current originates from the humidity-dependent impedance variation of the entire electrode/hydrogel/electrode system. Specifically, the humidity response arises from coupled ionic and electronic transport processes: hydrated pathways formed within the hydrogel promote ion migration, while the carboxylated MWCNT network provides electronic conduction. Ionic and electronic transport are not independent outputs but jointly determine the overall resistance and measured current of the sensor. The phenolic hydroxyl groups of TA and the carboxyl/carboxylate groups of SA and carboxylated MWCNTs provide hydrated sites and may participate in water-mediated proton transfer. In contrast, the amide groups of PAAm mainly contribute to water adsorption through hydrogen bonding rather than proton dissociation. Therefore, the sensing mechanism is attributed to bias-driven mixed ionic–electronic transport rather than to a single proton-conduction process.

Consistently, the RH-dependent EIS results show a continuous decrease in impedance with increasing relative humidity, indicating enhanced overall charge transport after hydration (Fig. 5(b)). Although EIS cannot quantitatively distinguish the individual ionic and electronic contributions, it supports the humidity-induced improvement in overall conductivity.

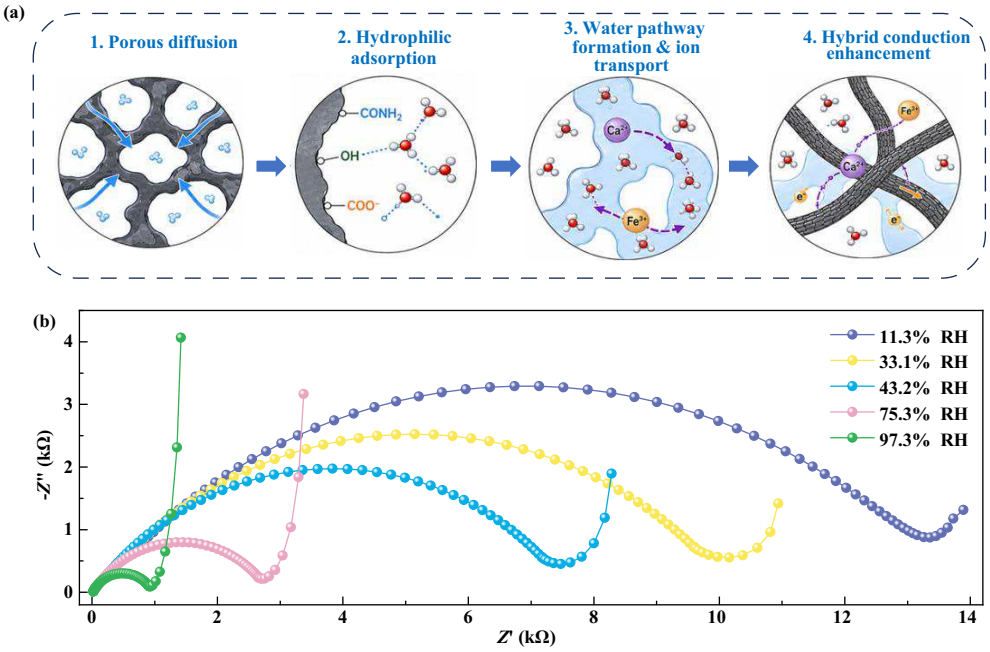

Fig. 5. (a) Schematic illustration of the humidity-sensing mechanism of the porous conductive triple-network hydrogel. (b) Nyquist plots of the sensor at relative humidity levels of 11.3%, 33.1%, 43.2%, 75.3%, and 97.3% RH.

3.5. Practical applications of the humidity sensor

3.5.1. Real-time respiratory monitoring

Respiratory frequency, depth, and rhythm reflect daily activity, respiratory function, and disease states. As shown in Fig. 6(a), the hydrogel sensor attached near a face mask recorded real-time respiration-induced current signals. As shown in Fig. 6(b), the sensor clearly distinguished three mouth-breathing modes. Deep breathing produced the largest $\Delta I/I_0$ peaks due to higher moisture output, normal breathing gave moderate peaks, and fast breathing exhibited higher frequency but lower amplitude. These distinct waveforms confirm that the sensor captures breathing patterns, rather than merely detecting humid airflow.

The representative traces yield respiratory rates of approximately 21, 33, and 55 breaths min^{-1} for deep, normal, and fast breathing, with corresponding peak $\Delta I/I_0$ values of approximately 230%, 105%, and 65%, respectively. These measurements demonstrate proof-of-concept breathing-pattern discrimination and respiratory-rate estimation under controlled conditions; they do not constitute clinical validation or establish diagnostic accuracy across subjects.

The sensor also responded differently to mouth and nose breathing. For mouth breathing, the response and recovery times were 0.287 s and 0.433 s, respectively (Fig. 6(d)); for nose breathing, they were 0.432 s and 0.575 s (Fig. 6(e)). The faster mouth response may result from the stronger and more direct humid airflow generated by oral exhalation, which accelerates water vapor adsorption and desorption at the sensing surface. These results demonstrate that the hydrogel sensor can resolve not only breathing rhythm but also differences in breathing pathways.

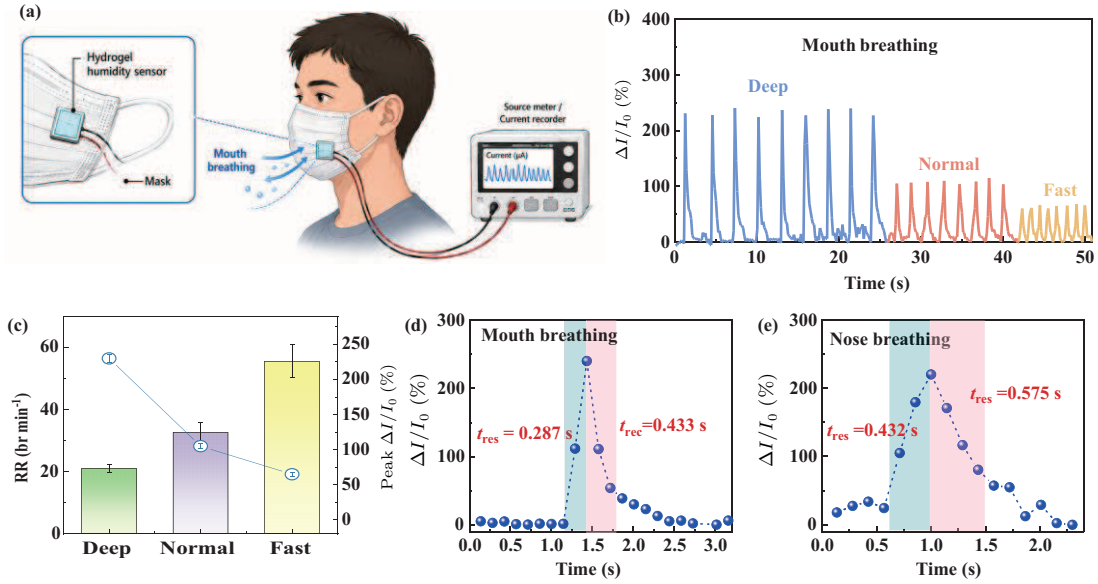

Fig. 6. (a) Sensor setup for breathing monitoring. (b) Current responses to three mouth-breathing modes. (c) Respiratory rate and amplitude. (d) Response and recovery times for mouth breathing. (e) Response and recovery times for nose breathing.

3.5.2. Non-contact humidity sensing and human–machine interaction

In addition to respiratory monitoring, the high sensitivity of the hydrogel sensor to local humidity variations makes it suitable for non-contact sensing applications, including hygienic human–machine interaction, touchless control, and intelligent electronic interfaces. Figure 7(a) schematically depicts a localized humidity field surrounding the fingertip and decreasing toward the sensor. We evaluated the non-contact response by repeatedly bringing a finger close to the sensor at distances of 2 mm, 3 mm, and 5 mm (Fig. 7(b)). The sensor produced clear and repeatable current signals without physical contact. The response was strongest at 2 mm, decreased at 3 mm, and remained detectable at 5 mm. This distance-dependent behavior is attributed to the gradual weakening of the local moisture gradient as the finger-sensor separation increases. The enlarged view of the response at 5 mm (Fig. 7(c)) further confirms that the sensor can still capture weak humidity perturbations at a relatively short range.

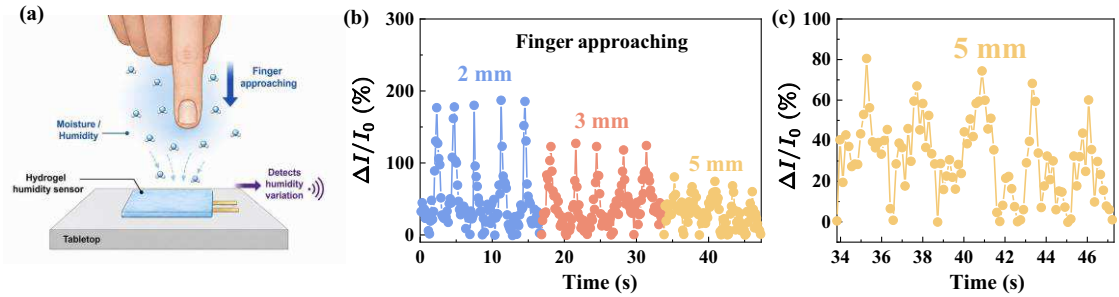

Fig. 7. (a) Schematic of non-contact sensing with a finger as a localized humidity source. The illustrated humidity field is schematic rather than a calculated concentration map. (b) Current responses upon finger approach at distances of 2, 3, and 5 mm. (c) Enlarged view of the response at 5 mm.

4. Conclusion

In summary, we have developed a porous conductive triple-network hydrogel for high-performance humidity sensing through the synergistic integration of structural engineering, electrical transduction, and mechanical reinforcement. The interconnected porous architecture provides rapid water vapor diffusion pathways. Carboxylated MWCNTs form a stable electronic conductive network, while the covalent PAAm, SA–Ca^{2+} ionic, and TA–Fe^{3+} coordination networks collectively suppress swelling and enhance mechanical stability. As a result, the sensor exhibits a wide detection range (11.3%–97.3% RH), an ultrafast response and recovery time of ≤ 0.144 s, and excellent cycling stability over 300 consecutive humidity cycles. Furthermore, it enables real-time differentiation of breathing patterns and pathways, as well as non-contact finger proximity detection at millimeter distances. This work demonstrates that the synergy of porous architecture, hybrid conductive pathways, and multi-network reinforcement provides a viable strategy for developing next-generation wearable humidity sensors and intelligent non-contact interfaces.

Acknowledgment

Project supported by the National Natural Science Foundation of China (Grant Nos. 12575041, 12504237, and 12405036).

References

[1] Xiang L, Zeng X, Xia F, Jin W, Liu Y and Hu Y 2020 *ACS Nano* **14** 6449
[2] Ma Y, Zhang Y, Cai S, Han Z, Liu X, Wang F, Cao Y, Wang Z, Li H, Chen Y and Feng X 2019 *Adv. Mater.* **32** 1902062
[3] Luo Y, Li J, Ding Q, Wang H, Liu C and Wu J 2023 *Nano-Micro Lett.* **15** 136
[4] Xiao C, Liu X, Zhao Y, Huang C, Zhou N and Mao H 2025 *Microsyst. Nanoeng.* **11** 221
[5] Lu Y, Yang G, Shen Y, Yang H and Xu K 2022 *Nano-Micro Lett.* **14** 150
[6] Zou S, Tao L Q, Wang G, Zhu C, Peng Z, Sun H, Li Y, Wei Y and Ren T L 2022 *ACS Appl. Mater. Interfaces* **14** 12606
[7] Yang J, Shi R, Lou Z, Chai R, Jiang K and Shen G 2019 *Small* **15** 1902801
[8] Yuk H, Lu B and Zhao X 2019 *Chem. Soc. Rev.* **48** 1642
[9] Liang Y, Ding Q, Wang H, Wu Z, Li J, Li Z, Tao K, Gui X and Wu J 2022 *Nano-Micro Lett.* **14** 183
[10] Wu J, Wu Z, Xu H, Wu Q, Liu C, Yang B R, Gui X, Xie X, Tao K, Shen Y, Miao J and Norford L K 2019 *Mater. Horiz.* **6** 595
[11] Liang A and Chen X 2024 *J. Mater. Chem. A* **12** 29081
[12] Wang W, Nayeem M O G, Wang H, Wang C, Kim J J, Wang B, Lee S, Yokota T and Someya T 2022 *Adv. Mater. Technol.* **7** 2200479
[13] Li T, Zhao T, Zhang H, Yuan L, Cheng C, Dai J, Xue L, Zhou J, Liu H, Yin L and Zhang J 2024 *npj Flex. Electron.* **8** 3
[14] Wang X, Deng Y, Chen X, Jiang P, Cheung Y K and Yu H 2021 *Microsyst. Nanoeng.* **7** 99
[15] Liu R, Liu Y, Fu S, Cheng Y, Jin K, Ma J, Wan Y and Tian Y 2024 *Small* **20** e2308092
[16] Guo Y, Xi H, Gu Z, Li M, Li X and Gao D 2023 *Colloids Surf. A* **658** 130700
[17] Guo W Y and Ma M G 2024 *J. Mater. Chem. A* **12** 9371
[18] Ji C, Wang Y, Qi Q, Li Y and Cao L 2025 *Adv. Mater. Technol.* **10** e01044
[19] Han M, Luo D, Talha K, He J, Xing M, Chen L and Liu H 2025 *J. Mater. Chem. A* **13** 18062
[20] Chu R, Liu W, Liu X, Yu D, Song Z, Li G and Wang H 2024 *ACS Appl. Nano Mater.* **7** 19355
[21] Zhao L, Ren Z, Liu X, Ling Q, Li Z and Gu H 2021 *ACS Appl. Mater. Interfaces* **13** 11344
[22] Liu Y, Zhang Z, Liang Z, Yong Y, Yang C and Li Z 2022 *J. Mater. Chem. A* **10** 16928
[23] Zhang X, Chen L, Zhang C and Liao L 2021 *ACS Appl. Mater. Interfaces* **13** 18175
[24] Sima H, Liu B, Shi X, Zhao Z, Liu C and Zhang C 2024 *Colloids Surf. A* **702** 135028
[25] Liu Z, Liu J, He S, Wu X, Wei X and Shao W 2024 *ACS Appl. Nano Mater.* **7** 7653
[26] Feng C, Cai L, Zhu G, Chen L, Xie X and Guo J 2025 *J. Colloid Interface Sci.* **677** 692
[27] Nicol E 2021 *Biomacromolecules* **22** 1325
[28] Wang Y K, Hu C, Li Z X, Zhao Q L, Wang H Y, Chen J H, Zheng D Z, Yang G Y and Liu B 2024 *Sens. Actuators B: Chem.* **410** 135655
[29] Gao Y, Jia F and Gao G 2022 *Chem. Eng. J.* **430** 132919
[30] Chen H, Huang X, Yang Y and Li Y 2024 *Nanomaterials* **14** 1694
[31] Fu Y, Yang C, Zhang B, Wan Z, Wang S, Zhang K, Yang L and Wei R 2024 *Adv. Funct. Mater.* **35** 2416453
[32] Cui Y, Du Y, Jia Y, Xu W, Bi Y, Xia X and Yang Q 2026 *Sens. Actuators B: Chem.* **448** 139062
[33] Wang Y S, Lou Y F, Xu P J, Wei W H, Yu Y, Feng Z S, Wan L Y, Kang F and Wang Y 2024 *Sens. Actuators B: Chem.* **418** 136316
[34] Ni Y, Zang X, Yang Y, Gong Z, Li H, Chen J, Wu C, Huang J and Lai Y 2024 *Adv. Funct. Mater.* **34** 2402853
[35] Xiao S, Lao Y, Liu H, Li D, Wei Q, Ye L and Lu S 2024 *ACS Sustainable Chem. Eng.* **12** 4464
[36] Zhou L, Zhang B, Zhou S, Zhou M, Li S, Shi Y, Gao Y, Lu X, Guo J and Zhang J 2025 *Phys. Scr.* **100** 095516
[37] Xia R L, Liu J, Shi J, He X D, Yuan J, Pike A R, Chu L, Wu Q and Liu B 2022 *Measurement* **201** 111781
[38] Ying B, Wu Q, Li J and Liu X 2020 *Mater. Horiz.* **7** 477
[39] Pan B, Su P, Jin M, Huang X, Wang Z, Zhang R, Xu H, Liu W and Ye Y 2023 *Mater. Horiz.* **10** 5263
[40] Cheng Y, Li L, Meredith C H, Balaj R V, Wang D, Pan M, Han T, Yang J, Wang Q, Dong L and Zarzar L D 2023 *ACS Mater. Lett.* **5** 2074
[41] Han Z, Zhu H and Cheng J H 2024 *Carbohydr. Polym.* **326** 121639
[42] Wu Z, Ding Q, Li Z, Zhou Z, Luo L, Tao K, Xie X and Wu J 2022 *Sci. China Mater.* **65** 2540
[43] Ding Q, Wang H, Zhou Z, Wu Z, Tao K, Gui X, Liu C, Shi W and Wu J 2022 *SmartMat* **4** e1147